mater.scichina.com link.springer.com

Published online 29 March 2021 | https://doi.org/10.1007/s40843-020-1612-y
Sci China Mater 2021, 64(9): 2202–2211

Topology conversion of 1T MoS_2 to S-doped 2H-$MoTe_2$ nanosheets with Te vacancies for enhanced electrocatalytic hydrogen evolution

Yaqian Wang[1†], Yongli Shen[2†], Xiong Xiao[2], Linxiu Dai[1], Shuang Yao[1*] and Changhua An[1,2*]

ABSTRACT **Metastable 1T' $MoTe_2$ has attracted much attention as a cost-effective electrocatalyst for hydrogen evolution reaction (HER) in recent years. However, few studies were done over common stable 2H phase because it often exhibits inferior performance. Herein, stable 2H $MoTe_2$ with S-doped Te vacancies has been synthesized by one-step telluride conversion of 1T MoS_2 at 700°C under Ar/H_2 atmosphere. It is demonstrated that the synergistic effect of S-doping and Te vacancies changes the electronic structures of the catalyst. Density functional theory (DFT) studies show that plentiful electrons accumulate on the surface S atoms in S-doped Te vacancies of 2H $MoTe_2$ catalyst, which may be as active sites to promote HER. Moreover, the as-synthesized catalyst can be directly used as working electrode, and realizes current density of 100 mA cm^{-2} at overpotential of 217 mV with Tafel slope of 94 mV dec^{-1}. This work stimulates intensive studies on the activation of inert phase of other nanocatalysts towards various reactions.**

Keywords: $MoTe_2$, defect, electrocatalysis, hydrogen evolution

INTRODUCTION

Hydrogen is a clean energy carrier bridging renewable energy and traditional fossil energy [1]. Precious metals, especially platinum (Pt) [2], have been the most efficient catalyst for hydrogen evolution reaction (HER). However, the high cost and scarcity of them on earth limit their practical applications [3]. The exploration of cost-effective electrocatalysts, i.e., transition metal/compounds [4,5], molecular catalysts [6,7], and carbon-based materials [8] with high efficiency is of paramount importance and highly desirable.

Two-dimensional (2D) transition metal dichalcogenides (TMDs) typically with formula of MX_2 (M = Mo/W; X = S/Se/Te) possess a variety of surprising properties [9], which enable them to be used in the fields of electronics/photonics [10], optoelectronics [11], sensing [12], energy storage [13], and catalysis [14,15]. In particular, the defect engineering [16,17], phase control [18,19], and coupling with other components [20,21] have been used to improve their HER activity. Recently, Wang *et al.* [22] reported a chemical etching strategy to introduce S vacancies on the surface of MoS_2 nanosheets, over which optimal HER reaches 131 mV overpotential at a current density of 10 mA cm^{-2}. Yang and co-workers [23] annealed bulk 2H-MoS_2 under an Ar/phosphorous vapor to produce 1T-2H MoS_2 heterostructures, exhibiting an overpotential of ~240 mV at 10 mA cm^{-2} in 1 mol L^{-1} KOH electrolyte. Reduced graphene oxide-modified $MoSe_2$ ($MoSe_2$/RGO) [24] showed the onset potential of HER at ~50 mV *vs.* reversed hydrogen electrode (RHE), which was much lower than that of bare $MoSe_2$ (150 mV). For $MoTe_2$, similar to Mo-S(Se)$_2$, it consists of alternately stacked Mo and Te layers that are connected by weak van der Waals interactions, in which three phases, namely 2H (hexagonal), 1T (triangular prism) and 1T′ (distorted-octahedral) phase are involved [25]. The smaller band gap and semi-metallic properties make it more promising in electrocatalysis in comparison with MoS(Se)$_2$ [26]. For example, a reversible activation of 1T'-$MoTe_2$ [27] results in the decrease of overpotential from 320 to 178 mV at 10 mA cm^{-2}. Controlled etching with a focused ion beam

[1] Life and Health Institute, Tianjin Key Laboratory of Organic Solar Cells and Photochemical Conversion, School of Chemistry and Chemical Engineering, Tianjin University of Technology, Tianjin 300384, China
[2] Tianjin Key Laboratory of Advanced Functional Porous Materials, Institute for New Energy Materials & Low-Carbon Technologies, School of Materials Science and Engineering, Tianjin University of Technology, Tianjin 300384, China
† These authors contributed equally to this work.
* Corresponding authors (emails: shuangyao@email.tjut.edu.cn (Yao S); anch@tjut.edu.cn (An C))

(FIB) patterning on chemical vapor deposition (CVD)-synthesized 1T′-$MoTe_2$ films creates active sites for the increase of HER [3]. Bottom-up phase engineering over 1T′ $MoTe_2$ and 1T′/2H $MoTe_2$ in CVD process was also developed to control the HER activity [28]. These progress mainly focuses on the modification of metastable metallic phase, and the current density is usually in a range of 10–60 mA cm^{-2} [29,30]. Considering the requirements in practice, the engineering of thermodynamically stable 2H $MoTe_2$ to realize HER at relatively large current density is more attractive.

Herein, an *in-situ* topology conversion of 1T MoS_2 nanosheets on nitrogen-doped carbon cloth (MoS_2/NCC) has been developed to produce S-doped 2H $MoTe_2$ nanosheets with rich Te vacancies (S-V_{Te}-2H $MoTe_2$/NCC). The as-prepared S-V_{Te}-2H $MoTe_2$/NCC can be directly applied as a free-standing electrode and yield a superior HER performance with an overpotential of 217 mV at the current density of 100 mA cm^{-2}, pushing the step towards practical application. The NCC substrate not only confines the growth of $MoTe_2$ nanosheets but also promotes complete contact between the active components and the electrolyte. These features allow H^+ ions to enter the active sites, thereby facilitate the charge transfer. Density functional theory (DFT) calculation reveals that the Te vacancies doping with S atoms could provide plentiful active sites, and make the Gibbs free energy closer to 0, thus boosting the HER activity.

EXPERIMENTAL SECTION

Chemicals and materials

All the chemicals were used as received without further purification. Carbon cloth (CC, HCP330N, 32 cm × 16 cm, thickness: 0.32 mm) was purchased from Shanghai Hesen Electric Co., Ltd. H_2NCONH_2 (Urea, AR, 99.0%, CAS: 57-13-6) was received from Sinopharm Chemical Reagent Co., Ltd. (Shanghai, China). Ammonium molybdate tetrahydrate ($H_{24}Mo_7N_6O_{24}{\cdot}4H_2O$, AR, CAS: 12054-85-2), *L*-cysteine ($HSCH_2CH(NH_2)CO_2H$, 99%, CAS: 52-90-4), and tellurium (Te, 99.99%, CAS: 13494-80-9) were obtained from Aladdin. Deionized water (18.25 MΩ) was applied for all experiments.

Materials synthesis

Preparation of NCC

Pure CC and urea with a mass ratio of 1:10 were put into a porcelain boat, which was heated to 700°C and reacted at that temperature for 3 h under ammonia atmosphere.

Hydrothermal synthesis of MoO_3 nanosheets

The MoO_3 nanosheets were synthesized following the reference [31]. Briefly, 0.9 g of $H_{24}Mo_7N_6O_{24}{\cdot}4H_2O$ was dissolved in 10 mL of ultrapure water. Then 4.5 mol L^{-1} nitric acid solution was added and stirred 10 min. The mixture was heated at 65°C in water bath for 3 h. After the reaction was complete, the resulting MoO_3 nanosheets were collected by centrifugation, washed with ethanol and distilled water three times. After being dried at 60°C in vacuum for 6 h, the sample was collected for the following use.

Synthesis of 1T MoS_2/NCC nanosheets

The as-obtained MoO_3 nanosheets (0.025 g) and $HSCH_2CH(NH_2)COOH$ (0.075 g) were dispersed in 15 mL ultrapure water with constant stirring 15 min. Then NCC was introduced, and the mixture was transferred to a 40-mL Teflon-lined stainless-steel autoclave. The reaction was carried out at 200°C for 12 h. The resulting MoS_2/NCC nanosheets were washed with ethanol/ultrapure water at least three times, and dried at 60°C for 8 h in vacuum.

Synthesis of S-V_{Te}-2H $MoTe_2$/NCC

The MoS_2/NCC and Te powder with a mass ratio of 1:5 were put into a porcelain boat, heated to 700°C at a rate of 5°C min^{-1} and maintained at that temperature for 5 h under argon-hydrogen (Ar/H_2 (H_2 10%)) atmosphere. In this process, MoS_2 nanosheets were successfully *in-situ* converted into S-V_{Te}-2H $MoTe_2$/NCC. For comparison, 2H $MoTe_2$/CC nanosheets were also prepared with a similar method.

Characterizations

The morphologies and microstructures of the samples were characterized by scanning electron microscopy (SEM; ZEISS MERLIN Compact), transmission electron microscopy (TEM) with FEG (Talos F200 X) instruments equipped with an Oxford SDD X-Max energy dispersive X-ray spectroscopy (EDS), and spherical aberration-corrected scanning TEM (SAC-STEM; FEI, Titan Themis Cubed G2 60-300). The crystal structure was analyzed by powder X-ray diffraction (XRD) on a Rigaku Corporation UItimaIV diffractometer using Cu Kα radiation (λ = 0.15418 nm). Raman spectra was conducted on a Renishaw-200 visual Raman microscope with a laser beam of 633 nm. X-ray photoelectron spectroscopy (XPS; ESCALAB 250 Xi, Thermo Scientific) was used to analyze the chemical composition of samples. The surface morphology and thickness of the nanosheets were measured

using atomic force microscope (AFM; NT-MDT). Electron paramagnetic resonance spectrometer (EPR; EMX-plus-6/1, Bruker) was used to confirm the existence of vacancies.

Electrochemical measurements

Electrocatalytic HER was carried out on an electrochemical workstation (CHI-760E, Shanghai Chenhua Company) in a standard three-electrode mode at room temperature. Saturated calomel electrode (SCE) and carbon electrode were used as the reference electrode and counter electrode, respectively. The electrolyte was 0.5 mol L^{-1} H_2SO_4. Linear sweep voltammetry (LSV) was conducted at a scan rate of 5 mV s^{-1}. The Tafel slope was obtained by fitting the linear portion of the Tafel plots following equation of ($\eta = a + b\log j$). Electrochemical impedance spectroscopy (EIS) was carried out from 0.01 to 10^5 Hz. All data were calibrated to the RHE with equation: $E_{(RHE, V)} = E_{(SCE, V)} + 0.059pH + 0.245$.

Computational method

All calculations presented in this work were performed using the Vienna *ab initio* Simulation Package (VASP) code [32,33]. The exchange-correlation functional was described according to the generalized gradient approximation (GGA)-Perdew, Burke and Ernzerhof (PBE) functional [34]. The electron wave function was expanded by plane waves with an energy cutoff of 400 eV. Energies and forces were converged to within 10^{-5} eV and 0.02 eV $Å^{-1}$, respectively. The (002) crystal face of 1T-MoS_2 and 2H-$MoTe_2$ have been modeled with unit cell of 1T-MoS_2 and 2H-$MoTe_2$ to represent the pristine MoS_2 and $MoTe_2$ surface. The S-doped (SD-MoX_2, X = S or Te in abbreviation) and S-doped-Te-vacancy (SDV-MoX_2, X = S or Te in abbreviation) MoS_2 and $MoTe_2$ catalysts were following 2 × 2 units cells of 1T-MoS_2 and 2H-$MoTe_2$. In all the models, three S-Mo-S (Te-Mo-Te) atom layers were included. In all calculations, the bottom atom layer of S-Mo-S (Te-Mo-Te) was fixed at their bulk positions and other layers together with the H atom were allowed to relax. The Brillouin zone was sampled by a *Γ*-centered *k*-point mesh generated through the Monkhorst-Pack method [35] with VASPKIT program [36]. The *k*-point-resolved value in VASPKIT was set to be 0.04 during all calculations.

RESULTS AND DISCUSSION

Fig. 1a schematically shows a typical procedure for the synthesis of S-V_{Te}-2H $MoTe_2$/NCC. Firstly, MoS_2/NCC (Figs S1–S3) was prepared by hydrothermal sulfidation of

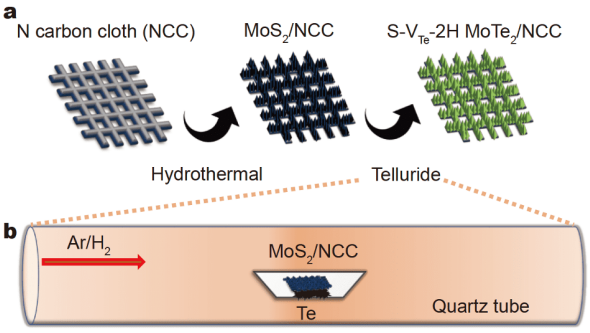

Figure 1 (a) Schematic illustration for the synthesis of S-V_{Te}-2H $MoTe_2$/NCC nanosheets. (b) Schematic cartoon of the reactor employed for the transformation of MoS_2/NCC to S-V_{Te}-2H $MoTe_2$/NCC.

MoO_3 nanosheets (Figs S4 and S5) with the assistance of NCC support. Then the obtained MoS_2/NCC was *in-situ* tellurized to 2H $MoTe_2$/NCC nanosheets at 700°C under Ar/H_2 atmosphere (Fig. 1b). In this process, abundant Te vacancies were generated and concurrently occupied by S atoms.

Fig. 2a shows the XRD pattern of the sample, where the diffraction peaks of (002), (004), (100), (103) can be indexed to the 2H $MoTe_2$, which shift to the high angle direction except (002) (in fact, it has a slight shift to low angle direction). The lattice parameters are separately estimated to be a = 3.440 Å, c = 13.998 Å. The value of a has a little contraction, and c is a little expansion in comparison with standard data (a = 3.519 Å, c = 13.964 Å, ICSD No. 72-0117)), implying that the lattice of the obtained sample has distortion to some extent. The prominent peaks in Raman spectra (Fig. S6) reveal out-of-plane A_{1g} (~168.4 cm^{-1}) and in-plane E^1_{2g} (~231.9 cm^{-1}) modes, respectively, further confirming that 2H $MoTe_2$ has been successfully synthesized [37]. The intensity of A_{1g} mode is much higher than that of E^1_{2g} mode, indicating its edge-terminated structure [38]. SEM images in Fig. 2b and AFM analysis in Fig. S7 show that $MoTe_2$ nanosheet arrays have lateral sizes of 200–500 nm and thickness of 8–10 nm on the NCC fiber support (Fig. S8) [39,40]. Raman spectra of C substrate (Fig. S9) shows a D band at 1350.3 cm^{-1} and G band at 1609.7 cm^{-1}, corresponding to the defective lattice with A_{1g} mode and graphitic lattice with E_{2g} vibration, respectively. The intensity ratio of D band *vs.* G band (I_D/I_G) is 1.015, showing the existence of disorder defects [41,42]. High-resolution TEM (HRTEM) image in Fig. 2c shows the as-grown $MoTe_2$ has a hexagonal structure with a lattice spacing of 0.31 nm, which is consistent with

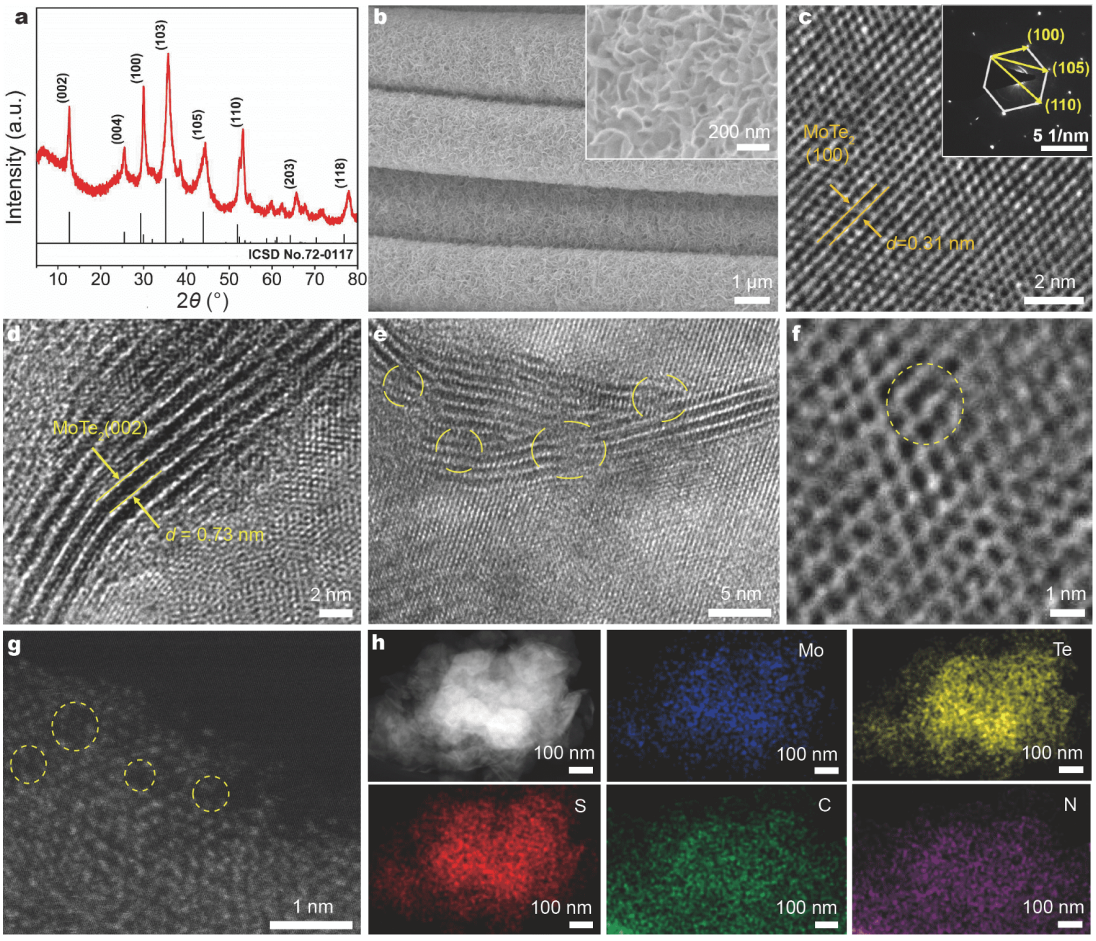

Figure 2 Structural characterizations of the as-obtained S-V_{Te}-2H $MoTe_2$/NCC nanosheets. (a) XRD pattern; (b) low- and high-magnification (inset) SEM images; (c–f) HRTEM images (the inset shows the SAED pattern); (g) the STEM image; (h) STEM-HAADF and corresponding elemental mapping images.

the (100) plane. The selected area electron diffraction (SAED) pattern demonstrates single-crystal nature of the sample (Fig. 2c). Fig. 2d shows typical HRTEM lattice fringe with spacing of 0.73 nm, featuring the (002) plane of 2H $MoTe_2$. The slightly expanded interlayer spacing indicates the lattice distortion induced by defects. This interlamellar expansion increases the activity of active sites and facilitates electron transport, thereby benefitting HER [43]. Moreover, unconnected broken lattices (Fig. 2e) imply the presence of abundant defects (namely, Te vacancies) on the surface of $MoTe_2$ nanosheets [44], which is highlighted with a yellow circle in Fig. 2f. SAC-STEM and EPR were also done to further prove the existence of Te vacancies. As shown in Fig. 2g, vacancies are randomly distributed on the sample surface. In EPR spectrum (Fig. S10), the characteristic peaks of the Mo–Te dangling bonds can be clearly detected at g = 1.99997, showing the paramagnetic signal from Te vacancies. The high-angle annular dark field (HAADF)-STEM image and elemental mappings confirm the homogeneous distribution of Mo, Te, S, C and N in the sample (Fig. 2h), implying successful doping of sulfur and nitrogen.

The surface composition and electronic state of the S-V_{Te}-2H $MoTe_2$/NCC arrays were investigated by XPS. The survey spectrum shown in Fig. S11 reveals the existence of Mo, Te, S, N, and C elements in the sample [45,46]. The atomic percentages of Mo, Te, S, N, and C elements are supplied in Fig. S12. In the high-resolution Mo 3d spectrum (Fig. 3a), the peaks at 228.75 eV (Mo $3d_{5/2}$) and 231.88 eV (Mo $3d_{3/2}$) for Mo–Te bonds shift towards higher binding energies compared with reported data [47,48]. The Mo–O bonds are from inevitable oxidation of $MoTe_2$ in air [49]. The binding energies at 573.3 and 583.69 eV are for the Te $3d_{5/2}$ and Te $3d_{3/2}$, respectively, corresponding to the Te–Mo bonds in the sample (Fig. 3b). Nevertheless, two peaks of Te–O in-

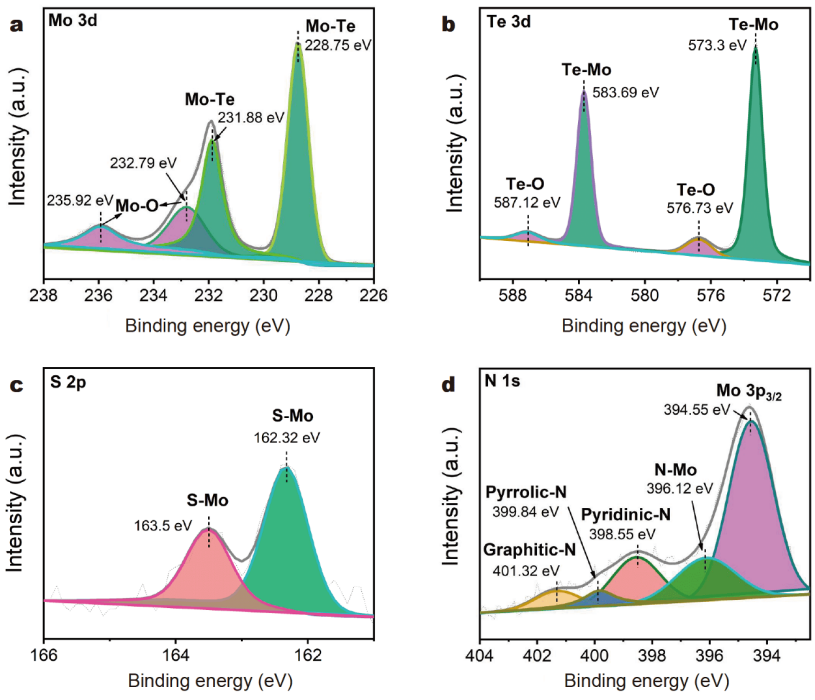

Figure 3 High-resolution XPS spectra of the respective elements in S-V_{Te}-2H $MoTe_2$/NCC. (a) Mo 3d; (b) Te 3d; (c) S 2p; (d) N 1s.

dicate the high oxidation state caused by increasing of Mo–Te dangling bonds [50]. The high-resolution S 2p spectrum in Fig. 3c clearly shows a doublet peak with the S $2p_{3/2}$ and S $2p_{1/2}$ at 162.32 and 163.5 eV, respectively, revealing the S–Mo bond in S-V_{Te}-2H $MoTe_2$/NCC. The N 1s peaks are partially overlapped with Mo 3p peaks and can be deconvoluted into four peaks (Fig. 3d). The peak at 396.12 eV corresponds to N 1s in the form of N–Mo bond [51], whereas the other three peaks at 398.55, 399.84 and 401.32 eV are assigned to pyridinic N, pyrrolic N and graphitic N, respectively [52,53]. The pyridinic N plays an essential role in the improvement of intrinsic activity of carbon materials, while graphitic N could boost the conductivity of substrates [53]. As observed in Fig. S13, the XPS peaks of C 1s are fitted to 284.8 and 286.1 eV, which are for the C–C/C=C, and C–N bonds, respectively, confirming the doped N into the CC [54]. The formation of Mo–N and C–N bonds demonstrates that $MoTe_2$ is anchored onto NCC by Mo–N–C bond, effectively stabilizing the catalyst.

To understand the impact of S-doped Te vacancies on the HER performance, the tests over different types of $MoTe_2$ were studied systematically. The steady-state LSV in N_2-saturated 0.5 mol L^{-1} H_2SO_4 (Fig. 4a) illustrates that the S-V_{Te}-2H $MoTe_2$/NCC exhibits an overpotential of 217 mV at large current density of 100 mA cm^{-2}, which is better than $MoTe_2$/CC (Fig. S14), MoS_2/NCC, and most reported similar catalysts (Table S1). Fig. 4b presents the overpotentials of these materials under various current densities (50, 100, and 150 mA cm^{-2}). The Tafel slope as a central kinetic parameter is usually used to investigate the rate-limiting step of an electrochemical process [55]. Here, the Tafel slope of the S-V_{Te}-2H $MoTe_2$/NCC is 94 mV dec^{-1}, as given in Fig. 4c, which is the smallest among all the samples. The electrochemical HER process in acidic medium can be divided into three steps [55]. (1) The Volmer reaction is an electrochemical hydrogen adsorption process ($H_3O^+ + e^- \rightarrow H^* + H_2O$), and the corresponding Tafel slope is about 120 mV dec^{-1}. (2) Heyrovsky reaction ($H^+ + H^* + e^- \rightarrow H_2$, also called electrochemical desorption) in the second step, or the (3) Tafel reaction ($H_{ads} + H^* \rightarrow H_2$, chemical desorption) in the third step, or the both can be used to generate H_2. When they are the rate-limiting steps, the Tafel slopes correspond to 40 and 30 mV dec^{-1}, respectively [56]. Herein, the obtained Tafel slope over our sample indicates a fast Heyrovsky-dominated Volmer-Heyrovsky mechanism. EIS tests were conducted from 100 kHz to 0.01 Hz to further investigate the electrode kinetics. Fig. 4d gives the Nyquist plots of these electrodes, where the diameter of semicircles represents the charge transfer resistance (R_{ct}) of H^+ reaction. Impressively, the R_{ct} of S-

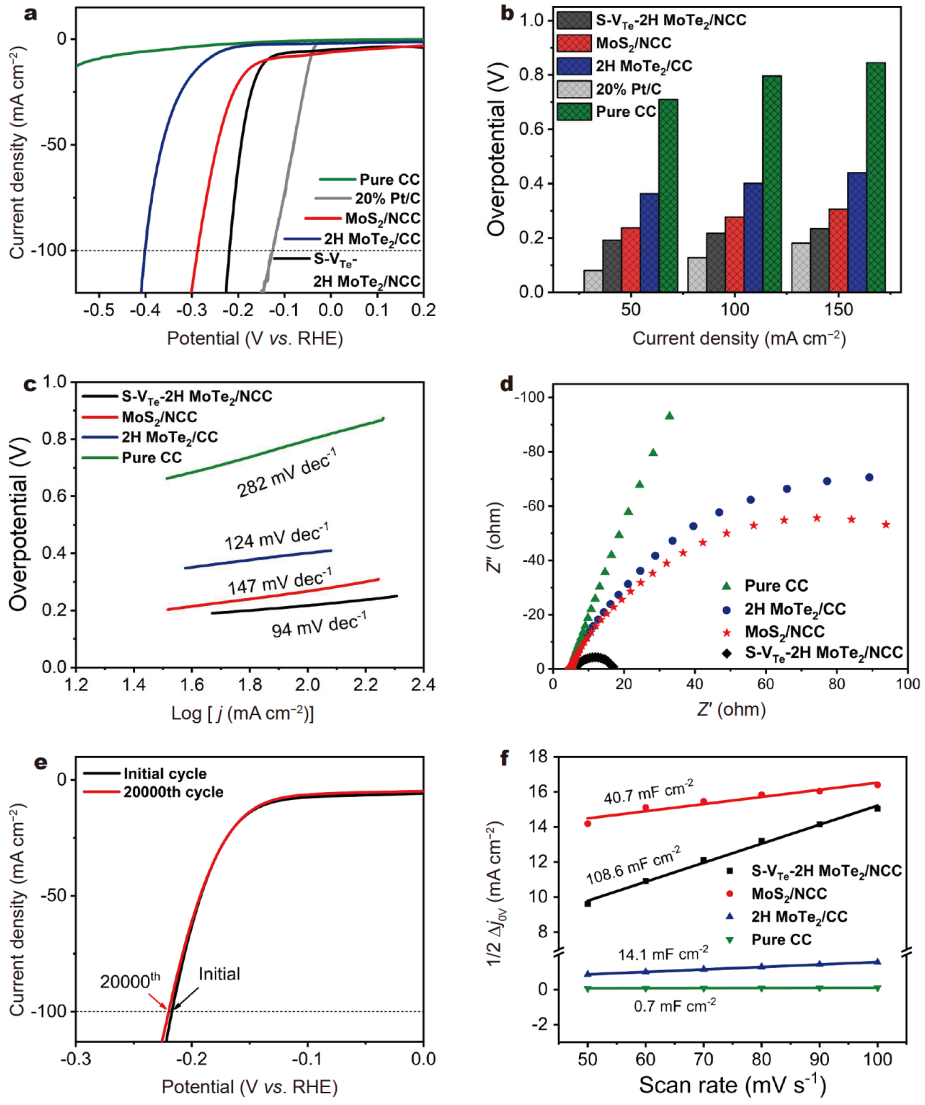

Figure 4 (a) Polarization curves of various catalysts in 0.5 mol L^{-1} H_2SO_4 with *iR* correction. (b) Comparisons of overpotentials required to deliver certain current densities over different catalysts. (c) Corresponding Tafel plots. (d) Nyquist plots in 0.5 mol L^{-1} H_2SO_4. (e) The initial, and 20,000th polarization curves of S-V_{Te}-2H $MoTe_2$/NCC nanosheets. (f) Electrochemical double-layer (C_{dl}) capacitance for the as-prepared materials.

V_{Te}-2H $MoTe_2$/NCC is much less than those of the other samples. These results demonstrate that the S-doped Te vacancies can greatly accelerate the charge transfer, thereby promoting electrical integration to reduce the parasitic ohmic loss and thus improving the reaction efficiency [22].

Stability is of crucial importance in electrocatalysis, and the commercially available electrode must maintain a stable current over a long period. As demonstrated in Fig. 4e, the polarization curve of S-V_{Te}-2H $MoTe_2$/NCC reveals a negligible change after 20,000 cycles in a range of −0.3–0 V *vs.* RHE at a scanning rate of 50 mV s^{-1}. Besides cyclic voltammetry (CV) cycles, current density *versus* time tests were also carried out (Fig. S15). Specifically, after 48 h fixed overpotential electrolysis, the current density of S-V_{Te}-2H $MoTe_2$/NCC retains well basically if the electrolyte refreshed every 24 h [57], further showing good stability at relatively high current density of 220–230 mA cm^{-2}. XRD and SEM of the collected sample after the test (Figs S16 and S17) reveal no obvious change in terms of morphology, structure, and phase. The XPS spectra (Fig. S18) of the sample after the durability test also show that the composition was not changed. To give more insights into the understanding of the improvement on the HER activity, the effective electrochemical active surface area (ECSA) [58] has been

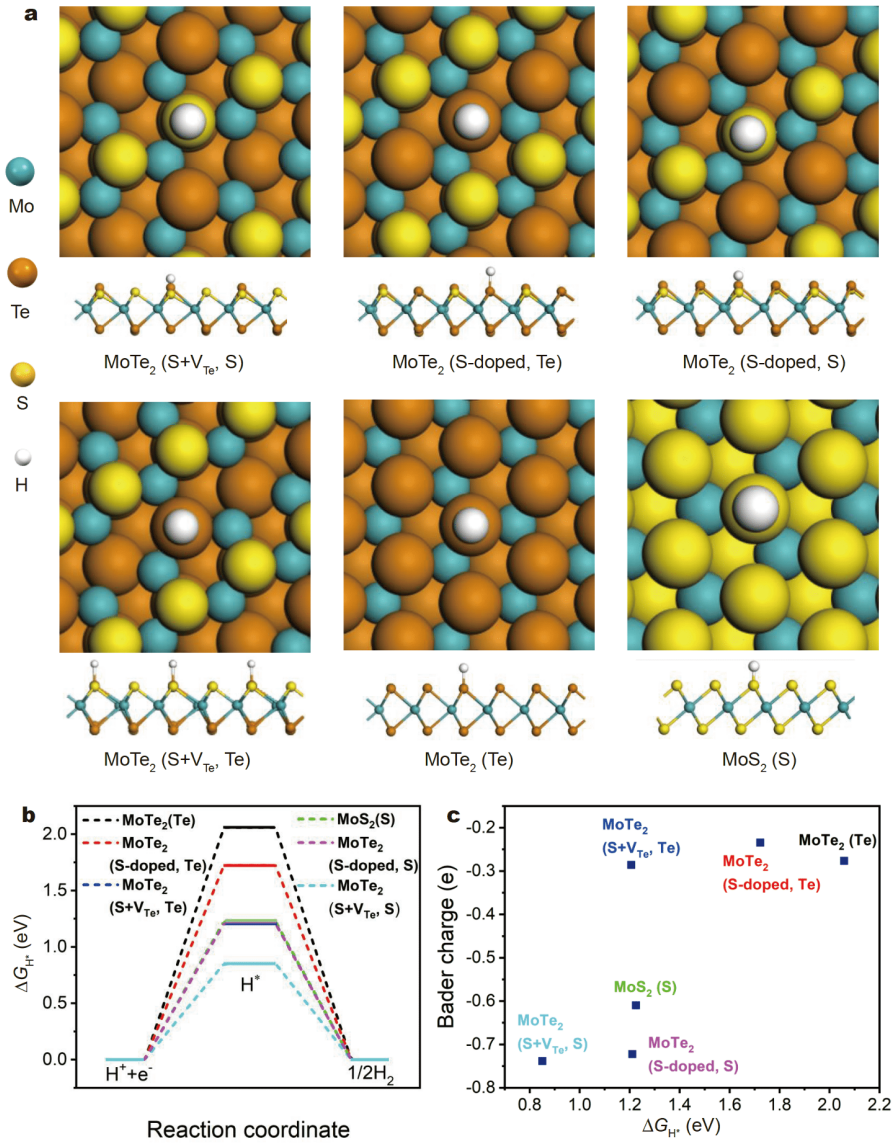

Figure 5 DFT calculations of S-V_{Te}-2H $MoTe_2$/NCC for HER. (a) The optimized on-top and side view structures of H adsorption on different sites on various doped catalysts. (b) The Gibbs free energy changes of HER on different catalysts. (c) The scatter diagrams of free energy change of HER *versus* Bader charge of related active sites of the catalysts.

estimated from the double-layer capacitance (C_{dl}) (Fig. 4f), which is determined by CV curves at scan rates from 50 to 100 mV s^{-1} (Fig. S19). The S-V_{Te}-2H $MoTe_2$/NCC delivers a high C_{dl} value up to 108.6 mF cm^{-2}, which is larger than that of 2H $MoTe_2$/CC (14.1 mF cm^{-2}) and MoS_2/NCC (40.7 mF cm^{-2}). Correspondingly, the ECSA of S-V_{Te}-2H $MoTe_2$/NCC is 3102.9 cm^{-2}, which is about three times that of MoS_2/NCC (1162.9 cm^{-2}). Therefore, it can be proposed that S-doped Te vacancies substantially boost the ECSA and the density of active sites. Meanwhile, the formation of Mo–N–C bonds between $MoTe_2$ and NCC endows the catalyst with good stability.

In order to understand the catalytic activity of S-V_{Te}-2H $MoTe_2$/NCC and clarify the catalytic nature, systematic theoretical calculation for HER on different catalyst surfaces were carried out. Because of the high electron density on the negatively charged atoms, the protons in the reaction system are more prone to adsorb on the negatively charged sites of the catalyst surface. Therefore, the surface S and Te atoms likely behave as the active sites of HER. Fig. 5a gives the most stable structure of H on different adsorption sites over doped catalysts.

The top and side views of the ball-and-stick structural models of H adsorption on different sites on various doped catalysts have been given in Fig. S20. Moreover, Tables S2–S7 exhibit all the original coordinate information files of the structures. To further study the co-effect of Te vacancies and S-doping in $MoTe_2$/NCC on the specific HER process, Fig. 5b and Fig. S21 show the Gibbs free energy changes (ΔG_{H^*}) of H adsorption on different active sites of $MoTe_2$ and S-V_{Te}-2H $MoTe_2$/NCC [2]. The results reveal that the free energy change of S-doped $MoTe_2$/NCC in S adsorption site is larger than that of S-V_{Te}-2H $MoTe_2$/NCC in S and Te adsorption sites, indicating that the S-V_{Te}-2H $MoTe_2$/NCC is more active than S-doped $MoTe_2$/NCC towards HER. When H is adsorbed at the S site of S-V_{Te}-2H $MoTe_2$/NCC, the free energy is the lowest, indicating S sites are easier to adsorb H^*. Therefore, we preliminarily infer that the synergistic effect of S-doping and Te vacancies may be the fundamental reason for improving the HER activity of $MoTe_2$. Then the Bader charge of the active sites of the catalysts was calculated. Plots of free energy change of HER *versus* Bader charge of related active sites of the catalyst exhibit a feature: the free energy change of HER basically has a positive correlation with the negative charge of the active sites. That is, the more negative the charge of the active site is, the stronger the activity is, basically coinciding with the linear relationship (Fig. 5c). In other words, the adsorption sites with more negative charges are more conducive to HER reaction. For the catalysts mentioned in this paper, there are more negative charges on the surface layer of S-V_{Te}-2H $MoTe_2$/NCC than on the surface of S-doped $MoTe_2$/NCC, which further indicates that S-doping and Te vacancies exert essential action on enhancing HER.

CONCLUSIONS

In summary, the hexagonal $MoTe_2$ nanosheets with Te vacancies occupied by S atoms confined with NCC have been synthesized by a simple *in-situ* conversion of 1T MoS_2/NCC under Ar/H_2 atmosphere. The results reveal that the doping of Te vacancies with S atoms to form Mo–S coordination can effectively modulate the local electronic structures of Te sites and S sites. As a result, the as-achieved S-V_{Te}-2H $MoTe_2$/NCC exhibits an overpotential of 217 mV at 100 mA cm^{-2} and displays a Tafel slope of 94 mV dec^{-1} towards HER. Meanwhile, it also exhibits long-term stability without obvious change at relatively large current density (220–230 mA cm^{-2}). The enhanced HER performance is due to the synergetic effect of Te vacancy and S doping, on which the adsorption sites have more negative charges, and facilitate HER. It is expected that the present work can be extended to engineering other TMDs towards specific applications.

Received 2 November 2020; accepted 8 January 2021; published online 29 March 2021

1 Dresselhaus MS, Thomas IL. Alternative energy technologies. Nature, 2001, 414: 332–337
2 Greeley J, Jaramillo TF, Bonde J, *et al.* Computational high-throughput screening of electrocatalytic materials for hydrogen evolution. Nat Mater, 2006, 5: 909–913
3 Zhuang P, Sun Y, Dong P, *et al.* Revisiting the role of active sites for hydrogen evolution reaction through precise defect Adjusting. Adv Funct Mater, 2019, 29: 1901290
4 Zhang C, Huang Y, Yu Y, *et al.* Sub-1.1 nm ultrathin porous CoP nanosheets with dominant reactive {200} facets: A high mass activity and efficient electrocatalyst for the hydrogen evolution reaction. Chem Sci, 2017, 8: 2769–2775
5 Wang P, Zhang X, Zhang J, *et al.* Precise tuning in platinum-nickel/nickel sulfide interface nanowires for synergistic hydrogen evolution catalysis. Nat Commun, 2017, 8: 14580
6 Karunadasa HI, Montalvo E, Sun Y, *et al.* A molecular MoS_2 edge site mimic for catalytic hydrogen generation. Science, 2012, 335: 698–702
7 Tran PD, Tran TV, Orio M, *et al.* Coordination polymer structure and revisited hydrogen evolution catalytic mechanism for amorphous molybdenum sulfide. Nat Mater, 2016, 15: 640–646
8 Zhao S, Wang DW, Amal R, *et al.* Carbon-based metal-free catalysts for key reactions involved in energy conversion and storage. Adv Mater, 2019, 31: 1801526
9 Manzeli S, Ovchinnikov D, Pasquier D, *et al.* 2D transition metal dichalcogenides. Nat Rev Mater, 2017, 2: 17033
10 Zhang Z, Chen P, Duan X, *et al.* Robust epitaxial growth of two-dimensional heterostructures, multiheterostructures, and superlattices. Science, 2017, 357: 788–792
11 Bi K, Wan Q, Shu Z, *et al.* High-performance lateral MoS_2-MoO_3 heterojunction phototransistor enabled by *in-situ* chemical-oxidation. Sci China Mater, 2020, 63: 1076–1084
12 Li BL, Wang J, Zou HL, *et al.* Low-dimensional transition metal dichalcogenide nanostructures based sensors. Adv Funct Mater, 2016, 26: 7034–7056
13 Chen L, Liu Y, Deng Z, *et al.* Edge-enriched MoS_2@C/rGO film as self-standing anodes for high-capacity and long-life lithium-ion batteries. Sci China Mater, 2021, 64: 96–104
14 Luxa J, Vosecký P, Mazánek V, *et al.* Layered transition-metal ditellurides in electrocatalytic applications—contrasting properties. ACS Catal, 2017, 7: 5706–5716
15 Sokolikova MS, Sherrell PC, Palczynski P, *et al.* Direct solution-phase synthesis of 1T' WSe_2 nanosheets. Nat Commun, 2019, 10: 712
16 Li H, Tsai C, Koh AL, *et al.* Activating and optimizing MoS_2 basal planes for hydrogen evolution through the formation of strained sulphur vacancies. Nat Mater, 2016, 15: 48–53
17 Ye G, Gong Y, Lin J, *et al.* Defects engineered monolayer MoS_2 for improved hydrogen evolution reaction. Nano Lett, 2016, 16: 1097–1103
18 Voiry D, Mohite A, Chhowalla M. Phase engineering of transition metal dichalcogenides. Chem Soc Rev, 2015, 44: 2702–2712

19 Xiao Y, Zhou M, Liu J, *et al.* Phase engineering of two-dimensional transition metal dichalcogenides. Sci China Mater, 2019, 62: 759–775
20 Li J, Hong W, Jian C, *et al.* High-performance hydrogen evolution at a $MoSe_2$-Mo_2C seamless heterojunction enabled by efficient charge transfer. J Mater Chem A, 2020, 8: 6692–6698
21 Wang Q, Zhao ZL, Dong S, *et al.* Design of active nickel single-atom decorated MoS_2 as a pH-universal catalyst for hydrogen evolution reaction. Nano Energy, 2018, 53: 458–467
22 Wang X, Zhang Y, Si H, *et al.* Single-atom vacancy defect to trigger high-efficiency hydrogen evolution of MoS_2. J Am Chem Soc, 2020, 142: 4298–4308
23 Wang S, Zhang D, Li B, *et al.* Ultrastable in-plane 1T-2H MoS_2 heterostructures for enhanced hydrogen evolution reaction. Adv Energy Mater, 2018, 8: 1801345
24 Tang H, Dou K, Kaun CC, *et al.* $MoSe_2$ nanosheets and their graphene hybrids: Synthesis, characterization and hydrogen evolution reaction studies. J Mater Chem A, 2014, 2: 360–364
25 Huang HH, Fan X, Singh DJ, *et al.* Controlling phase transition for single-layer MTe_2 (M = Mo and W): Modulation of the potential barrier under strain. Phys Chem Chem Phys, 2016, 18: 4086–4094
26 Tan Y, Luo F, Zhu M, *et al.* Controllable 2H-to-1T′ phase transition in few-layer $MoTe_2$. Nanoscale, 2018, 10: 19964–19971
27 McGlynn JC, Dankwort T, Kienle L, *et al.* The rapid electrochemical activation of $MoTe_2$ for the hydrogen evolution reaction. Nat Commun, 2019, 10: 4916
28 Lu D, Ren X, Ren L, *et al.* Direct vapor deposition growth of 1T′ $MoTe_2$ on carbon cloth for electrocatalytic hydrogen evolution. ACS Appl Energy Mater, 2020, 3: 3212–3219
29 Tan C, Luo Z, Chaturvedi A, *et al.* Preparation of high-percentage 1T-phase transition metal dichalcogenide nanodots for electrochemical hydrogen evolution. Adv Mater, 2018, 30: 1705509
30 Sun K, Zeng L, Liu S, *et al.* Design of basal plane active MoS_2 through one-step nitrogen and phosphorus co-doping as an efficient pH-universal electrocatalyst for hydrogen evolution. Nano Energy, 2019, 58: 862–869
31 Li JB, Chen X, Wu FG, *et al.* Preparation method for molybdenum trioxide nanosheets and gas-sensitive detector manufactured from molybdenum trioxide nanosheets. China Invention Patent, 2016, CN 201610121080.5
32 Kresse G, Furthmüller J. Efficient iterative schemes for *ab initio* total-energy calculations using a plane-wave basis set. Phys Rev B, 1996, 54: 11169–11186
33 Kresse G, Furthmüller J. Efficiency of *ab-initio* total energy calculations for metals and semiconductors using a plane-wave basis set. Comput Mater Sci, 1996, 6: 15–50
34 Perdew JP, Burke K, Ernzerhof M. Generalized gradient approximation made simple. Phys Rev Lett, 1996, 77: 3865–3868
35 Monkhorst HJ, Pack JD. Special points for Brillouin-zone integrations. Phys Rev B, 1976, 13: 5188–5192
36 Wang V, Xu N, Liu JC, *et al.* VASPKIT: A pre- and post-processing program for VASP code. ArXiv, 1908.08269v5, 2019
37 Park JC, Yun SJ, Kim H, *et al.* Phase-engineered synthesis of centimeter-scale 1T′- and 2H-molybdenum ditelluride thin films. ACS Nano, 2015, 9: 6548–6554
38 Zhang Z, Li W, Yuen MF, *et al.* Hierarchical composite structure of few-layers MoS_2 nanosheets supported by vertical graphene on carbon cloth for high-performance hydrogen evolution reaction. Nano Energy, 2015, 18: 196–204
39 Zhao Y, Zhang X, Jia X, *et al.* Sub-3 nm ultrafine monolayer layered double hydroxide nanosheets for electrochemical water oxidation. Adv Energy Mater, 2018, 8: 1703585
40 Zhao Y, Jia X, Chen G, *et al.* Ultrafine NiO nanosheets stabilized by TiO_2 from monolayer NiTi-LDH precursors: An active water oxidation electrocatalyst. J Am Chem Soc, 2016, 138: 6517–6524
41 Pachfule P, Shinde D, Majumder M, *et al.* Fabrication of carbon nanorods and graphene nanoribbons from a metal-organic framework. Nat Chem, 2016, 8: 718–724
42 Wang JY, Ouyang T, Li N, *et al.* S, N co-doped carbon nanotube-encapsulated core-shelled CoS_2@Co nanoparticles: Efficient and stable bifunctional catalysts for overall water splitting. Sci Bull, 2018, 63: 1130–1140
43 Seok J, Lee JH, Cho S, *et al.* Active hydrogen evolution through lattice distortion in metallic $MoTe_2$. 2D Mater, 2017, 4: 025061
44 Yao K, Xu Z, Huang J, *et al.* Bundled defect-rich MoS_2 for a high-rate and long-life sodium-ion battery: Achieving 3D diffusion of sodium ion by vacancies to improve kinetics. Small, 2019, 15: 1805405
45 Cho JS, Ju HS, Lee JK, *et al.* Carbon/two-dimensional $MoTe_2$ core/shell-structured microspheres as an anode material for Na-ion batteries. Nanoscale, 2017, 9: 1942–1950
46 Shan TT, Xin S, You Y, *et al.* Combining nitrogen-doped graphene sheets and MoS_2: A unique film-foam-film structure for enhanced lithium storage. Angew Chem Int Ed, 2016, 55: 12783–12788
47 Yoo Y, DeGregorio ZP, Su Y, *et al.* In-plane 2H-1T′ $MoTe_2$ homojunctions synthesized by flux-controlled phase engineering. Adv Mater, 2017, 29: 1605461
48 Zhang X, Jin Z, Wang L, *et al.* Low contact barrier in 2H/1T′ $MoTe_2$ in-plane heterostructure synthesized by chemical vapor deposition. ACS Appl Mater Interfaces, 2019, 11: 12777–12785
49 Zhou L, Xu K, Zubair A, *et al.* Role of molecular sieves in the CVD synthesis of large-area 2D $MoTe_2$. Adv Funct Mater, 2017, 27: 1603491
50 Xia B, Wang T, Jiang X, *et al.* Ar^{2+} beam irradiation-induced multivancancies in $MoSe_2$ nanosheet for enhanced electrochemical hydrogen evolution. ACS Energy Lett, 2018, 3: 2167–2172
51 Zhang Y, Ouyang B, Xu J, *et al.* 3D porous hierarchical nickel-molybdenum nitrides synthesized by RF plasma as highly active and stable hydrogen-evolution-reaction electrocatalysts. Adv Energy Mater, 2016, 6: 1600221
52 Chen YY, Zhang Y, Jiang WJ, *et al.* Pomegranate-like N,P-doped Mo_2C@C nanospheres as highly active electrocatalysts for alkaline hydrogen evolution. ACS Nano, 2016, 10: 8851–8860
53 Wang H, Xiao X, Liu S, *et al.* Structural and electronic optimization of MoS_2 edges for hydrogen evolution. J Am Chem Soc, 2019, 141: 18578–18584
54 Lv Z, Tahir M, Lang X, *et al.* Well-dispersed molybdenum nitrides on a nitrogen-doped carbon matrix for highly efficient hydrogen evolution in alkaline media. J Mater Chem A, 2017, 5: 20932–20937
55 Zhu J, Hu L, Zhao P, *et al.* Recent advances in electrocatalytic hydrogen evolution using nanoparticles. Chem Rev, 2020, 120: 851–918
56 Zhang Z, Wang Y, Leng X, *et al.* Controllable edge exposure of MoS_2 for efficient hydrogen evolution with high current density. ACS Appl Energy Mater, 2018, 1: 1268–1275
57 Zhang X, Zhao Y, Zhao Y, *et al.* A simple synthetic strategy toward defect-rich porous monolayer NiFe-layered double hydroxide nanosheets for efficient electrocatalytic water oxidation. Adv Energy Mater, 2019, 9: 1900881

58 Zhang XL, Hu SJ, Zheng YR, *et al.* Polymorphic cobalt diselenide as extremely stable electrocatalyst in acidic media *via* a phase-mixing strategy. Nat Commun, 2019, 10: 5338

Acknowledgements This work was supported by the National Natural Science Foundation of China (21771137).

Author contributions An C conceived the whole project; Wang Y and An C designed the strategy; Wang Y performed the experiments and wrote the draft; Shen Y conducted the theoretical simulations; Xiao X took part in the characterizations of samples; Wang Y and Xiao X analyzed the data and discussed the results; Dai L and Yao S discussed the data and revised the draft.

Conflict of interest The authors declare that they have no conflict of interest.

Supplementary information Supporting data are available in the online version of the paper.

Yaqian Wang received her BSc degree from Hebei Normal University for Nationalities in 2018. Now she is a Master student under the supervision of Dr. Shuang Yao, and Prof. Changhua An at the School of Chemistry and Chemical Engineering, Tianjin University of Technology (TUT). Her main research interest is the synthesis and modification of 2D TMDs in electrocatalysis.

Yongli Shen obtained his PhD degree in the College of Chemistry, Nankai University, in 2009, and then worked at the School of Chemical Engineering and Technology, Tianjin University as a postdoctoral researcher from 2009–2012. He joined TUT in 2015. His research focuses on catalysis and applied quantum chemistry.

Shuang Yao is an associate professor at TUT. She received her PhD degree from the Faculty of Chemistry, Northeast Normal University in 2011. Her current research focuses on the metal-cluster-based photocatalytic materials.

Changhua An received his PhD degree from the University of Science and Technology of China (USTC) in 2003 with Prof. Yitai Qian. After he did postdoc with Prof. Taeghwan Hyeon at Seoul National University from 2004 to 2005, he joined China University of Petroleum as an associate professor. In 2013, he was promoted to full professor of materials science and chemistry. From 2016, he has been a Tianjin distinguished professor at TUT. His research interests focus on the synthesis, characterization, and explorations of efficient catalysts in the fields of clean energy production and environmental purification.

拓扑转化1T MoS_2为硫掺杂碲空位的$MoTe_2$纳米片及其增强电催化氢析出

王雅倩[1†], 申勇立[2†], 肖雄[2], 代林秀[1], 姚爽[1*], 安长华[1,2*]

摘要 本文在Ar/H_2气氛中通过原位转化1T MoS_2法合成出一种负载型$MoTe_2$纳米片. 其表征结果说明, 反应过程中硫引入到$MoTe_2$纳米片, 同时产生了碲空位, 使得电化学比表面积增大, 活性位点增多; 硫掺杂和碲空位的协同作用促进了H^*的吸附及H_2的析出. 氮掺杂碳负载的硫掺杂含碲空位的$MoTe_2$可直接用作工作电极, 在217 mV过电位下实现了100 mA cm^{-2}的电流密度, 塔菲尔斜率为94 mV dec^{-1}. 催化剂在酸性电解质中表现出优异的稳定性, 优于多数已报道的$MoTe_2$电催化剂. 该工作为优化其他半导体惰性纳米催化剂提供了思路.

